

Topical Review

Spin waves in disordered materials

Paweł Buczek¹, Stefan Thomas², Alberto Marmodoro³, Nadine Buczek⁴,
Xabier Zubizarreta², Martin Hoffmann⁵ , Timofey Balashov⁶ ,
Wulf Wulfhekel⁶, Khalil Zakeri^{2,7}  and Arthur Ernst^{2,5}

¹ Hochschule für Angewandte Wissenschaften Hamburg, Fakultät Technik und Informatik, Berliner Tor 7, 20099 Hamburg, Germany

² Max Planck Institute of Microstructure Physics, Weinberg 2, 06120 Halle, Germany

³ Department Chemie, Physikalische Chemie, Universität München, Butenandstraße 5-13, D-81377 München, Germany

⁴ Hochschule Lübeck, Fachbereich Angewandte Naturwissenschaften, Mönkhofer Weg 239, 23562 Lübeck, Germany

⁵ Institute for Theoretical Physics, Johannes Kepler University Linz, Altenberger Straße 69, 4040 Linz, Austria

⁶ Physikalisches Institut, Karlsruhe Institute of Technology, Wolfgang-Gaede-Strasse 1, D-76131 Karlsruhe, Germany

⁷ Heisenberg Spin-dynamics Group, Physikalisches Institut, Karlsruhe Institute of Technology, Wolfgang-Gaede-Strasse 1, D-76131 Karlsruhe, Germany

E-mail: martin.hoffmann@jku.at and arthur.ernst@jku.at

Received 11 June 2018, revised 30 August 2018

Accepted for publication 5 September 2018

Published 27 September 2018



CrossMark

Abstract

We present an efficient methodology to study spin waves in disordered materials. The approach is based on a Heisenberg model and enables calculations of magnon properties in spin systems with disorder of an arbitrary kind and concentration of impurities. Disorder effects are taken into account within two complementary approaches. Magnons in systems with substitutional (uncorrelated) disorder can be efficiently calculated within a single-site coherent potential approximation for the Heisenberg model. From the computation point of view the method is inexpensive and directly applicable to systems like alloys and doped materials. It is shown that it performs exceedingly well across all concentrations and wave vectors. Another way is the direct numerical simulation of large supercells using a configurational average over possible samples. This approach is applicable to systems with an arbitrary kind of disorder. The effective interaction between magnetic moments entering the Heisenberg model can be obtained from first-principles using a self-consistent Green function method within the density functional theory. Thus, our method can be viewed as an *ab initio* approach and can be used for calculations of magnons in real materials.

Keywords: spin wave, magnon, disorder, impurity, *ab initio*

(Some figures may appear in colour only in the online journal)

1. Introduction

Spin waves (or magnons) are low-lying collective excitations (quasiparticles) of the electronic spin structure in a crystal lattice [1–3] and each of these excitations corresponds to a reduction in the total magnetization of the system by $2\mu_B$, which is

manifested as a deviation of the atomic moments from their equilibrium directions [4]. Magnons are bosons, carry a fixed amount of energy ω and a lattice momentum, and cover a very wide frequency window from gigahertz to a few hundred terahertz. Hence, they contribute to many observed phenomena, e.g. magnetic ordering [5], ultrafast magnetization processes

[6], electronic specific heat [7], electrical and thermal conductivity [8], current induced magnetization reversal, and electron spin dynamics [9]. Besides these phenomena, various coupling mechanisms with electrons and phonons in magneto-caloric materials [10] and in high-temperature superconductors [11–14] can be caused by spin waves.

Magnons can be probed with various experimental methods like inelastic neutron scattering [15, 16], inelastic photon scattering [17, 18], scanning tunneling spectroscopy (STS) [19–22], spin-wave resonances [23], and spin-polarized electron energy loss spectroscopy (SPEELS) [4, 24–33]. The most recent development in this research field was achieved for low-dimensional systems. In particular, SPEELS and STS allow the investigation of magnetic excitations in nanostructures such as thin films, clusters, chains, and adatoms. These experiments enable direct measurements of the magnon dispersion relation, lifetime, group and phase velocities. Several low-dimensional systems have efficiently been studied by these methods in the last decade, for example, thin Fe, Co, Ni, Mn films on Cu(001), W(110), Pd(001), Rh(001), Ir(001), and Cu₃Au(001) surfaces. A particular high energy resolution became possible with a new electron spectrometer for unpolarized electrons [34–36], which enables the study of spin waves with less than 3 meV resolution in the wave vector range between 1 nm⁻¹ and 3 nm⁻¹ [37, 38]. In this range, thin film standing modes are observed in addition to the acoustic mode [39]. Furthermore, the lifetime of spin waves increases with the inverse fourth power of the wave vector, which make these spin waves candidates for magnon-based devices [37].

The rapid progress and success of these experiments inspired the development of new theoretical approaches, which are specially designed to study magnetic excitations in complex and extended materials. One class of these methods is based on mapping the spin system onto an effective Heisenberg Hamiltonian. This approach is utilized in many different forms like the magnetic force theorem [40], static transverse susceptibility [41, 42], frozen magnon techniques [43], and atomistic spin dynamics [44–48]. In combination with the density functional theory, such methods do not involve adjustable parameters and are applicable to a wide range of material classes.

Another way to access magnetic excitations is the direct calculation of the transverse magnetic susceptibility, whose poles are associated with magnons and yield the magnon energies and life times. The magnetic susceptibility can be obtained within the linear response density functional theory [49, 50], which offers a transparent parameter free approach in order to obtain both—spin waves and Stoner excitations. This method is implemented within several numerical schemes and successfully applied to study magnons in complex bulk and low dimensional materials [51–59].

However, we have also to take into account that the real systems are imperfect. Structural defects, impurities, or alloying can substantially modify the structural, electronic and magnetic properties of the host materials. One way to model such systems is the use of a large number of large periodic supercells where disorder is approximated by randomly

generated atomic configurations in the supercells. This method allows direct studies of arbitrary disorder, although it is very demanding with respect to computing time. An alternative approach is the coherent potential approximation (CPA), which is a mean-field theory and designed for studies of substitutionally disordered alloys [60]. Subsequently, it was suggested to use the Green function method also to study the electronic structure of impurities and defects in various host materials [61]. Therein, the Green function of an impurity or an ensemble of atoms embedded in a particular system can be determined in an elegant way by solving a Dyson equation, which is associated with the host material via a reference Green function. Both the supercell approach and the CPA are widely used for first-principles studies of various properties of solids. In this work, we concentrate on spin waves or magnons in disordered materials. Thereby, two main aspects will be taken into account: the impact of disorder on (i) the electronic structure and magnetic interactions and (ii) the spin waves of the disordered systems. The first aspect can be efficiently treated within a standard single-site CPA approach using a self-consistent Green function method, which provides magnetic moments and exchange interaction of the disordered system from first-principles. This information can then be further used for the calculation of the second aspect—magnons—considering disorder effects either within the supercell approach or the CPA method formulated for the magnonic Green function or the transversal susceptibility. The later can be utilized either within the Heisenberg model [62–67] or computed directly using time dependent density functional theory combined with the CPA [54].

In the current work, we focus on the second aspect and present our technique to calculate spin waves in disordered materials, which is realized with both the supercell and the CPA approaches [68]. The starting point is the adiabatic spin dynamics based on the mapping of the magnetic states onto the states of the Heisenberg Hamiltonian. From the Heisenberg model, the magnetic susceptibility can be calculated either in the real space and then subsequently averaged over different disorder configurations, or it can be obtained within the CPA implemented for complex unit cells, which might contain also various types of chemical or magnetic disorder.

The paper is organized as follows: The transverse magnetic susceptibility within the adiabatic approximation is introduced in section 2. Subsequently, we present our model for describing magnons in disordered systems within the real space supercell approach and the CPA method in sections 3 and 4, respectively. In section 5, we discuss briefly our method for the calculation of the exchange parameters entering the Heisenberg Hamiltonian. The efficiency of our technique is illustrated for several examples in sections 3 and 4.

2. Transverse magnetic susceptibility

The interaction of the spins will be described in terms of the classical Heisenberg Hamiltonian. This effective Hamiltonian relates the existing spins at sites i and j with the magnetic exchange constants J_{ij}

$$H = -\frac{1}{2} \sum_{ij} J_{ij} \mathbf{e}_i \cdot \mathbf{e}_j, \quad (1)$$

where \mathbf{e}_i and \mathbf{e}_j are the directions of the spin moments at the sites i and j , respectively. Spin waves (or magnons) are then low energy excitations associated with small-amplitude precessions of the spin moments around the equilibrium direction and, in the case of ferromagnets, can be described by the retarded transverse magnetic susceptibility $\chi_{ij}(\omega + i0^+)$ (0^+ stands for an infinitesimal positive quantity) [58]. The susceptibility relates the amplitude of the precession of the spin moment at the site i around its ground state direction to the time dependent transverse (i.e. orthogonal to the ground state magnetization direction) magnetic field applied at site j , while ω stands for the frequency of the field and the linear magnetic response.

We evaluate the susceptibility starting from the following expression

$$\chi = gGS, \quad (2)$$

where g is the electron g -factor (assumed to be equal to 2 in this work) and G and S are matrices in the space of atomic sites. Moreover, S is diagonal and given by the magnetic moments S_i of the constituting atoms

$$S_{ij} = S_i \delta_{ij}. \quad (3)$$

G is called the *magnon spin propagator*

$$G(z) = G_0(z) + G_0(z)gSTG, \quad (4)$$

$$G_0(z) = \mathbb{1}z^{-1}, \quad (5)$$

where z stands for the complex frequency, $\mathbb{1}$ is the unit matrix, G_0 denotes the *free spin propagator* and the *torque matrix* T is evaluated as follows

$$(ST)_{ij} = S_j^{-1} \delta_{ij} \sum_l J_{il} - S_i^{-1} J_{ij}. \quad (6)$$

The formal solution of (4) can be obtained by matrix inversion

$$G^{-1} = G_0^{-1} - gST, \quad (7)$$

which in turn yields the susceptibility upon applying (2).

The loss matrix [58]

$$\mathcal{L}\chi(\omega + i0^+) = \frac{1}{2i} \left[\chi(\omega + i0^+) - \chi(\omega + i0^+)^{\dagger} \right], \quad (8)$$

gives the spectral density of the magnon excitations at the given energy ω and the corresponding eigenvectors give the spatial form of these excitations. The calculations of the average susceptibility and the corresponding loss matrix in disordered magnets as well as the subsequent analysis of the resulting magnonic excitation spectra are the main theoretical tools of this paper. This is achieved by averaging the susceptibility $\chi(\omega + i0^+)$ over a number of differently occupied supercells (called configurations) or by solving corresponding CPA equations.

3. Numerical averaging of magnons in real space

The transverse magnetic susceptibility can be directly calculated in real space for a supercell \mathbf{R}^{sc} , which is a fragment of

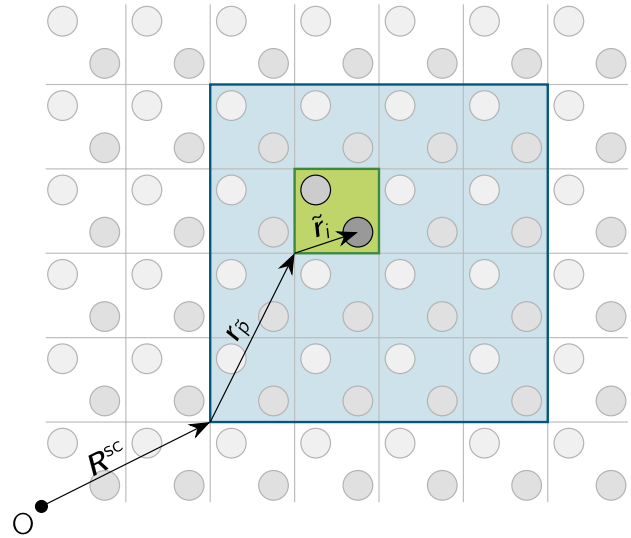


Figure 1. Definition of coordinates. The simulation domain is a supercell (blue) with its origin being located at \mathbf{R}^{sc} . It consists of unit cells (green) at $\mathbf{r}_{\bar{p}}$ with respect to the origin of the supercell and the unit cells may contain several basis atoms (circles) at $\tilde{\mathbf{r}}_i$.

an infinite crystal (figure 1). Each position i of the crystal is occupied by atoms of types α, β, \dots with some given probabilities $c_{i\alpha}, c_{i\beta}, \dots$. We introduce the occupation function $p^\alpha(\mathbf{r}_i)$, which is 1, if the site is occupied by the atom of the type α , and 0 otherwise. The disorder is called uncorrelated, if the occupation of one site does not influence the occupation of the other sites. The atomic occupation in the supercell \mathbf{R}^{sc} is chosen with respect to the probabilities $c_{i\alpha}$. The susceptibility of the disordered system $\langle \chi \rangle$ is then obtained by averaging over many such configurations (typically between 100 and 1000 created using pseudorandom numbers).

A general extension to this algorithm is the introduction of an additional subdivision of the supercell \mathbf{R}^{sc} into basis sites α in a cell \bar{p} (figure 1) by splitting the vectors as

$$\mathbf{r}_i = \mathbf{R}^{\text{sc}} + \mathbf{r}_{\bar{p}} + \tilde{\mathbf{r}}_i. \quad (9)$$

Afterwards, it is possible to fold the supercell back to the original unit cell by application of a Fourier transformation

$$\langle \chi_{ij}(\mathbf{q}) \rangle = \sum_{\bar{p}} \sum_{\tilde{i}} e^{i\mathbf{q} \cdot \mathbf{r}_{\bar{p}}} e^{-i\mathbf{q} \cdot \tilde{\mathbf{r}}_i} \langle \chi_{(\bar{p},i),(\tilde{i},j)}(\mathbf{q}) \rangle, \quad (10)$$

where \mathbf{q} is the wave vector from the first Brillouin zone and the sums run over all unit cells \bar{p} and \tilde{i} .

3.1. Generation of realistic structures

The generation of random structures, i.e. different occupations of the simulated supercells, is a critical part in the calculation of the susceptibility of disordered systems and plays an important role in the success of the method. The main goal of the following algorithms is to resemble real physical structures as closely as possible [69].

Especially for surface structures, it is important to find reasonable methods, because the growth process will impact the resulting structures: For example, seven monolayers (ML) of Co deposited on Cu(001) yield a rugged surface structure with

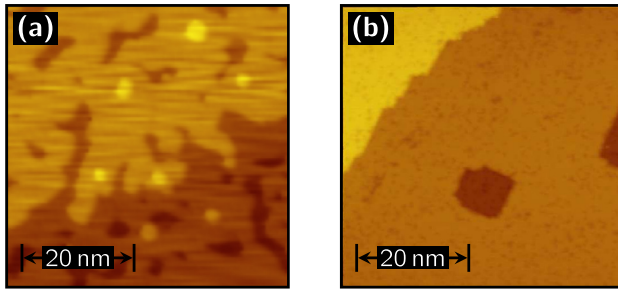


Figure 2. Scanning tunneling microscopy (STM) images of (a) as-deposited 7 ML Co/Cu(1 0 0), (b) Co/Cu(1 0 0) after annealing at 370 K. Different colors denote different surface heights. Reproduced with permission from [70].

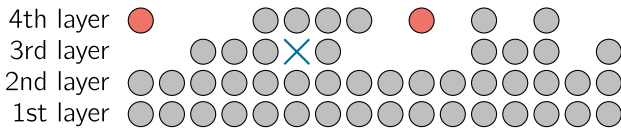


Figure 3. Side view of a possible random configuration of a 3 ML thick film, where 50% of the atoms from the third layer are moved to the fourth layer. Possibly undesired floating atoms (red) and holes (blue cross) were created.

several different thicknesses and plateaus with diameters of a few nm (figure 2(a)). To reduce the impact of this disorder, the sample was annealed at 370 K to obtain a much smoother surface (see figure 2(b)) [70]. However, since films with less than six monolayers of Co on Cu(1 0 0) suffer from diffusion of Cu to the surface, while annealing [70], the rugged structures are a necessary target for the structure generation algorithm. For the simulation of smooth annealed surfaces, an algorithm capable of avoiding a surplus amount of point defects would be favorable.

In the following, three major algorithms are presented, which were used for the creation of random structures. They are focused on performance and tunability of the resulting outputs. Because of their versatility and good comparison with the shown experimental surfaces, they were chosen over more complex algorithms, like kinetic Monte Carlo approaches.

Although the supercell approach allows in principle to consider also local lattice relaxations in the structure, we restrict ourself for the examples below to experimental lattice structures and parameters. We study only the effect of substitutional disorder, which was the main focus of this work and a large size of the used supercells would raise the computational costs beyond feasibility. An additional effect of local relaxations on the magnonic spectrum will depend on the system and has to be verified separately.

3.1.1. Direct random structure generation and Fisher–Yates–Shuffle. The most straightforward approach to create random structures is the use of standard pseudorandom numbers (PRN). A given setup and equally distributed PRNs in the right-open interval $[0..1)$ —the output of most standard PRN generators—offer two basic ways to create the desired random distribution of atoms.

The first method is the direct use of the random numbers by dividing the interval according to the probabilities of each

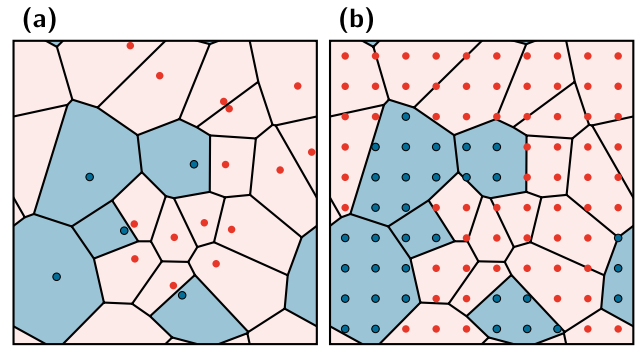


Figure 4. Example of two dimensional Voronoi tessellation with two different species (red and blue). (a) The dots represent the initial points P_k . The corresponding Voronoi regions R_k (separated by black lines) get the same lighter color (same species) as the P_k inside that region. (b) Resulting distribution of atom species from Voronoi tessellation in (a). All other points (basis sites of the supercell) are now assigned with the respective color of their region (reddish or bluish).

species at a given site. For example, a probability of 40% for species A and 60% for species B would result in species A for all random numbers $p < 0.4$ and species B, otherwise. An important caveat of this method is the possibility of an unbalanced system, where the actual final composition does not meet the desired probabilities (if at all possible due to the limited amount of lattice positions in the supercell). In this case, an additional rebalancing step might be necessary.

The second method is the use of the Fisher–Yates–Shuffle [71]:

Algorithm 1. Fisher–Yates–Shuffle.

Require: $a(1 : n)$ contains desired composition
for $i = n$ **downto** 2 **do**
 $j \leftarrow$ random integer $1 \leq j \leq i$
 swap $a(i) \leftrightarrow a(j)$
end for

For a given site in the original unit cell, a list of all corresponding positions in the supercell is created and filled with the desired composition of species in an arbitrary order. Applying the above example to a system with 25 sites would result in a list filled with 10 entries of A and 15 entries of B. Then, the Fisher–Yates–Shuffle will create a completely random permutation of this composition, which can then be used for further calculations.

Nevertheless, both methods can produce non-physical or undesired results. A calculation of a 3 ML system, where 50% of sites from the third layer are moved to the fourth layer (figure 3), will for example most likely produce floating atoms or holes.

3.1.2. Random structures from Voronoi tessellation. This method is based on a Voronoi tessellation of the supercell in order to create the desired distribution of atoms. At first, some points P_k (which get marked with a species label) are put into the supercell and the Voronoi tessellation (with cyclical boundary conditions) is computed (figure 4(a)). The initial sites P_k were distributed within a uniform distribution and

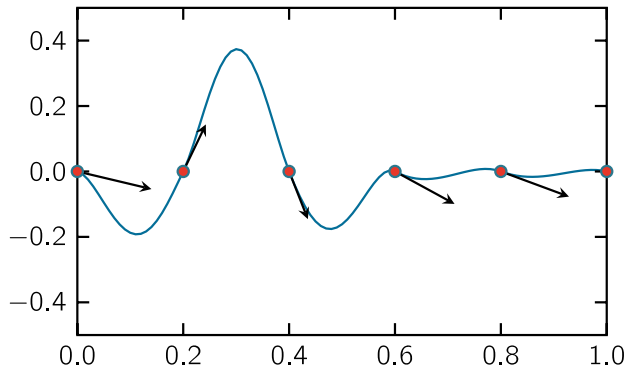


Figure 5. Example for one dimensional Perlin noise (blue line). The low-resolution grid is defined at the red points and the gradient vectors are represented by arrows.

the corresponding atomic type is assigned randomly according to the desired concentration. The Voronoi regions R_k get then the same species label as the corresponding initial points \mathbf{P}_k . In the next step, the atoms in the supercell get assigned the appropriate species, determined by the species label of the Voronoi region at the corresponding position (figure 4(b)).

Similar to the other methods, additional steps are needed to get the desired stoichiometry. This can be achieved using a weighted Voronoi tessellation and optimizing the weights w_k towards the desired composition:

$$R_k = \{\mathbf{x} \in \mathbb{R}^n \mid d(\mathbf{x}, k) \leq d(\mathbf{x}, j), \forall j \neq k\}, \quad (11)$$

$$d(\mathbf{x}, k) = w_k \cdot \|\mathbf{x} - \mathbf{P}_k\|_2. \quad (12)$$

Due to the fact that the Voronoi regions are defined by the points in the supercell, there are no limitations to the shape of the supercell. Additionally, the size of the generated structures (i.e. clusters of similar atoms) can be tuned by the composition and amount of the initial points \mathbf{P}_k .

3.1.3. Perlin method. The third possible method is based on the popular Perlin noise [72, 73], which is commonly used for procedural creation of textures in computer graphics. The idea of this approach is to model the surface in terms of a smooth noise function. Some form of downsampling is applied to create a closed hilly surface which can be used in susceptibility calculations.

In order to create Perlin noise on a grid (in this case, the supercell), a second grid with a lower resolution is generated and its vertices are populated with random gradient vectors. Then, for every point in the supercell, i.e. the high-resolution grid, the contributions from the nearest gradient vectors are weighted to get a smooth noise function. In the one dimensional case, the gradients from the vertices to the left and to the right are used and the resulting linear functions are interpolated (figure 5). In the two dimensional case, the interpolation would be calculated from the four vertices of the circumscribing rectangle.

In figure 5, it becomes apparent that this definition of Perlin noise results in the value ‘zero’ at each of the low-resolution grid’s vertices. For that reason, an additional contribution of cubically interpolated regular noise, which is also defined at

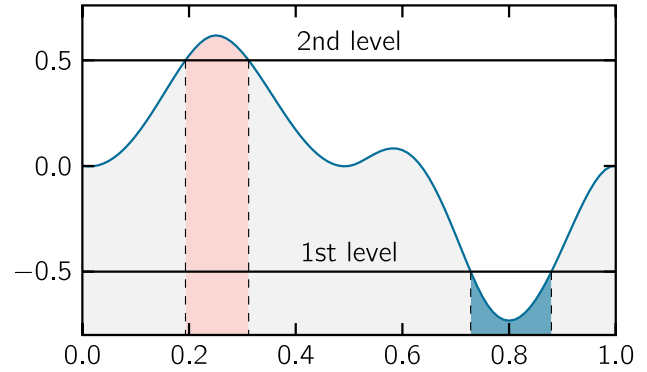


Figure 6. Level-set method with two levels at 0.5 and -0.5 applied to one dimensional Perlin noise. The blue area is below the first level, the gray areas between both levels and the red area is above the second level.

the vertices of the low-resolution grid, was added to the Perlin noise. The generation of the final structure from the Perlin noise is then achieved with the help of a level-set method (figure 6). In this method, one or more thresholds are defined and compared to the noise function at every position in the grid.

The example in the figure can be interpreted as a one dimensional surface. Positions, where the noise function is less than the first level, would get assigned no atoms, positions with a value between the two levels get assigned one atom and positions with a value above the second level get assigned two atoms.

This method has the same problems concerning stoichiometry as the purely random distribution of atoms. To get closer to the desired composition, the thresholds of the level set method can be adapted to fit the needs of the calculation. Another problem is the fact that this method can only be defined on a rectangular grid. As a result, the application of Perlin noise to a non-rectangular supercell, which is needed for calculations of, e.g. a hexagonal surface represented by rhombic unit cells, would result in a distorted grid with a strong anisotropy. In particular, one diagonal of the unit cell is longer than the other resulting in a structure, which is stretched along the longer diagonal. A possible solution is provided by simplex noise [74], a later invention of [73], which is defined on a triangular grid.

3.2. Application of the Perlin method to thin films

From the properties of the three methods, it is straightforward to determine which method should be used for a given system [69]: The two dimensional systems, i.e. such as 7 ML Co/Cu(001) (figure 2) or similar, could be created with the Perlin method. Depending on the size of the surface’s features, a varying resolution of the coarse grid can be used. While the annealed system can be obtained from the algorithm as described, the unannealed system could be generated with a high-resolution ‘coarse’ grid to effectively switch of its smoothing capability. On the other hand, a purely random composition might produce acceptable results for the unannealed structure, but this was not used in actual calculations.

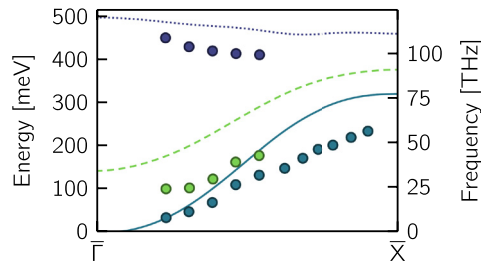


Figure 7. Magnons in the ordered 3 ML Co/Cu(001) calculated using the Heisenberg model (lines) and compared with the results of the SPEELS measurements (dots) [87]. Frequency range is estimated by $E = hf$ with Planck's constant h .

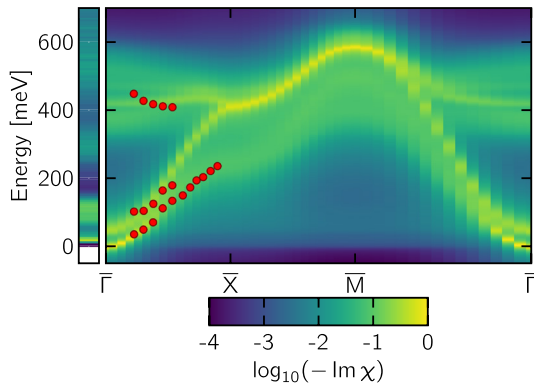


Figure 8. Calculated magnons in 3 ML Co/Cu(001) shown as contour plot together with the results of the SPEELS measurements (dots) [87] and the STS measurements (inset at $\bar{\Gamma}$ -point on the left). Direct numerical averaging, supercells created with the Perlin method and the structural model similar to the structure shown in figure 3 were used.

For demonstration, we calculated at first the spin waves in an ordered 3 ML Co film on a Cu(001) surface (assuming ideal growth conditions) and compared with SPEELS measurements, whose experimental details are described in [4, 33] (figure 7). Indeed, the theory cannot reproduce correctly the acoustic mode in higher wave vectors, although the agreement for lower energies and small wave vectors is rather well. The first optical branches are substantially overestimated by the theory for all wave vectors, especially for the lowest optical mode. Hence, we applied the Perlin method to create more realistic supercells and calculated again the spin waves in 3 ML Co/Cu(001) for rugged surface configurations like those shown in figure 3. This structure was elucidated from the recent STM measurements by Balashov [70]. The supercell consisted of 32×32 unit cells of the surface structure with the experimental lattice constant of Cu continued also for the 3 ML of Co. The calculated magnetic susceptibility within this structural model is in very good agreement with experimental results, including STS measurements (figure 8). However, the spin wave energies can be also significantly modified by the presence of islands, which could arise during growth processes.

As another example, we studied magnons in the disordered system of 1 ML of Fe on a Pd(001) surface. The growth of this system depends strongly on the deposition temperature [75]. Varying the deposition temperature one obtains various

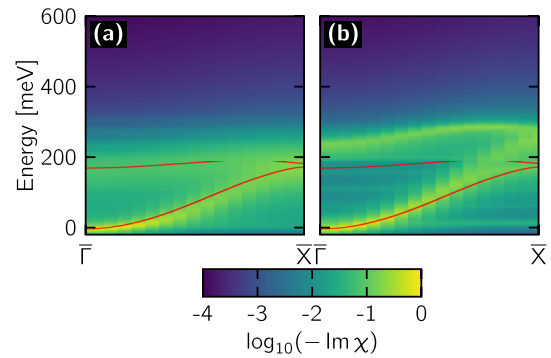


Figure 9. Spin-wave spectra of 1 ML Fe on Pd with an actual composition of $(\text{Fe}_{0.7}\text{Pd}_{0.3} | \text{Fe}_{0.3}\text{Pd}_{0.7})$ for the surface and first subsurface layer, respectively: (a) for a purely random structure and (b) for a structure with islands. Continuous red lines represent the VCA calculations for this alloy.

alloy configurations in the surface and the first subsurface layers. At certain conditions, Fe and Pd atoms are not mixed randomly but forming small islands within the surface double layer. Such clustering increases magnon energies for larger wave vectors (figure 9). For comparison, we calculated also spin waves using a so called virtual crystal approximation (VCA), which reproduces rather good results for the purely random structure (red lines in figure 9).

We conclude this section with two statements.

- We observed that the character of disorder/order is a very fundamental aspect for both two dimensional examples. Random distribution or a certain amount of short-range order can alter the spin-wave spectra dramatically. The same holds true for three dimensional systems. If the atoms of the different species are randomly distributed, a purely random generation is preferred, and if a clustering of similar atoms is observed, the Voronoi tessellation is the method of choice. In the latter case, a three dimensional variant of the Perlin method would also be possible, but this was not implemented because of the limitations apparent from the two dimensional version.
- On the other hand, we note that metallic thin film systems show often a clear separation of surface/interface and bulk magnonic modes. The acoustic modes in the Co/Cu(001) result clearly from the surface because the reduced coordination number of Co atoms at the interface or surface drastically changes the magnetic exchange constants as shown for Fe/Ir(001) layers by Zakeri *et al* [76]. They show that the lowest magnon modes result from the varied magnetic exchange interactions at the surface or interface.

4. CPA for the Heisenberg model

In this section, we report on the semi-analytic CPA of the Heisenberg model. The approach is applicable when the substitutional disorder is not spatially correlated. We followed the formalism suggested by Matsubara [62] and Yonezawa [77] taking into account the off-diagonal disorder

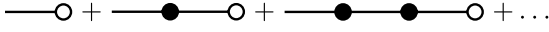


Figure 10. Expansion of the $\chi_{ij}^{\alpha\beta}(z, \mathbf{q}, \mathbf{q}')$ susceptibility.

as suggested by Blackman, Esterling, and Berk (BEB) [78]. Several realizations of the Heisenberg model within the BEB approach were proposed over the last 50 years [63, 64, 67]. Although the implementations of the method by different authors differ in details, the foundation of all works on the Heisenberg-CPA are similar. Our implementation based on the derivation by Matsubara and Yonezawa is unique in the sense that it has been generalized for the case of complex unit cells, arbitrary number of atomic species forming the disordered system, and arbitrary dimensionality.

The coherent potential approximation for the transverse magnetic susceptibility of the Heisenberg Hamiltonian involves the following steps. The *species resolved Fourier transformation of the susceptibility* is defined as

$$\chi_{ij}^{\alpha\beta}(\mathbf{q}, \mathbf{q}') = \sum_{\mathbf{R}\mathbf{R}'} p^{\alpha i}(\mathbf{R}) e^{-i\mathbf{q}\cdot\mathbf{R}} \times \chi(\mathbf{R} + \tilde{\mathbf{r}}_i, \mathbf{R}' + \tilde{\mathbf{r}}_j) p^{\beta j}(\mathbf{R}') e^{i\mathbf{q}'\cdot\mathbf{R}'}, \quad (13)$$

where the notation of vectors is similar as in figure 1 but in contrast to (10) we consider only unit cells \mathbf{R} . The occupation function defined in section 3 is written as $p^{\alpha i}(\mathbf{R}) := p^\alpha(\mathbf{R} + \tilde{\mathbf{r}}_i)$ to simplify the notation. Equation (13) yields the Fourier transform of the full susceptibility

$$\chi_{ij}(\mathbf{q}, \mathbf{q}') = \sum_{\alpha\beta} \chi_{ij}^{\alpha\beta}(\mathbf{q}, \mathbf{q}'). \quad (14)$$

The susceptibility above describes a single random realization of the random supercell.

Following (4), the susceptibility in the real space becomes an infinite sum of scattering terms

$$\chi(z) = G_0 g S + G_0 g S T G_0 g S + G_0 g S T G_0 g S T G_0 g S + \dots, \quad (15)$$

where the ST product is defined by (6).

The Fourier transformation $\chi_{ij}^{\alpha\beta}(z, \mathbf{q}, \mathbf{q}')$ can be computed term-by-term and diagrammatically represented as in figure 10. Each diagram is constructed from three elements described below. Each of the elements is a matrix in a composite space of basis sites and atomic species. For simplicity, we resort to the following notation $(i) \equiv i\alpha$, $(j) \equiv j\beta$, $(l) \equiv l\gamma$, $(m) \equiv m\mu$, etc. Furthermore, the Einstein summation convention is used. The three constituting elements are:

- (i) \mathcal{T} -matrix denoted with filled circle (●)

$$\mathcal{T}_{ij}^{\alpha\beta}(\mathbf{q}, \mathbf{q}') = \rho^{(l)}(\mathbf{q} - \mathbf{q}') \tau_{(i)(j)}^{(l)}(\mathbf{q}, \mathbf{q}'), \quad (16)$$

where

$$\tau_{(i)(j)}^{(l)}(\mathbf{q}, \mathbf{q}') \equiv g S_\beta^{-1} \left[J_{jl}^{\beta\gamma}(\mathbf{q} - \mathbf{q}') \delta_{(i)(j)} - J_{ij}^{\gamma\beta}(\mathbf{q}') \delta_{(i)(l)} \right], \quad (17)$$

$$\rho^{i\alpha}(\mathbf{q}) \equiv \sum_{\mathbf{R}} p^{\alpha i}(\mathbf{R}) e^{-i\mathbf{q}\cdot\mathbf{R}}, \quad (18)$$

$$J_{ij}^{\alpha\beta}(\mathbf{q}) \equiv \sum_{\mathbf{R}} J_{ij}^{\alpha\beta}(\mathbf{R}) e^{-i\mathbf{q}\cdot\mathbf{R}}. \quad (19)$$

The two latter quantities are the lattice Fourier transformed occupation function and exchange parameters, respectively.

- (ii) \mathcal{S} -matrix denoted with open circle (○)

$$\mathcal{S}_{(i)(j)}(\mathbf{q}, \mathbf{q}') = \rho^{(l)}(\mathbf{q} - \mathbf{q}') \sigma_{(i)(j)}^{(l)}, \quad (20)$$

$$\sigma_{(i)(j)}^{(l)} \equiv g \delta_{(i)(j)} \delta_{(i)(l)} S_{(l)}. \quad (21)$$

- (iii) Propagator of uncoupled magnetic moments (—)

$$\Gamma_{(i)(j)}(z) = z^{-1} \delta_{(i)(j)}. \quad (22)$$

This matrix does not depend on the momentum. It depends on the frequency and, as a matter of fact, it is responsible for the frequency dependence of the CPA self energy.

The diagrams' evaluation rules are:

- (i) The matrices in the $(i)(j)$ space in a diagram are matrix-multiplicated in this space.
- (ii) Every internal free propagator line involves an integration over the Brillouin zone, with a simplified notation

$$\frac{1}{\Omega_{\text{BZ}}} \int_{\mathbf{q} \in \Omega_{\text{BZ}}} f(\mathbf{q}) d\mathbf{q} \equiv \int_{\mathbf{q}} f(\mathbf{q}). \quad (23)$$

As an example, let us consider the second term in the sum including the product of two random variables $\rho^{(i)}(\mathbf{q})$. Its expansion is graphically represented in figure 10 and explicitly written as

$$\begin{aligned} \chi_{ij}^{\alpha\beta}(z, \mathbf{q}, \mathbf{q}') &= z^{-2} \int_{\mathbf{q}_1} \mathcal{T}_{(i)(m)}(\mathbf{q}, \mathbf{q}_1) \mathcal{S}_{(m)(j)}(\mathbf{q}_1, \mathbf{q}'), \\ &= z^{-2} \rho^{(l_1)}(\mathbf{q} - \mathbf{q}_1) \tau_{(i)(m)}^{(l_1)}(\mathbf{q}, \mathbf{q}_1) \\ &\quad \times \rho^{(l_2)}(\mathbf{q}_1 - \mathbf{q}') \sigma_{(m)(j)}^{(l_2)}. \end{aligned} \quad (24)$$

(Einstein convention is used for the indices (l_1) , (l_2) , and (m) .)

In the next step, the averaged susceptibility is computed. The averaging restores the translational symmetry of the system and the susceptibility depends only on one wave vector variable

$$\langle \chi_{ij}^{\alpha\beta}(z, \mathbf{q}, \mathbf{q}') \rangle \equiv \langle \chi_{ij}^{\alpha\beta}(z, \mathbf{q}) \rangle \Omega_{\text{BZ}} \delta(\mathbf{q} - \mathbf{q}'). \quad (25)$$

In what follows, we will arrive at the coherent potential approximation for $\langle \chi_{ij}^{\alpha\beta}(z, \mathbf{q}) \rangle$. We average every term of the expansion from figure 10 separately. Following Yonezawa

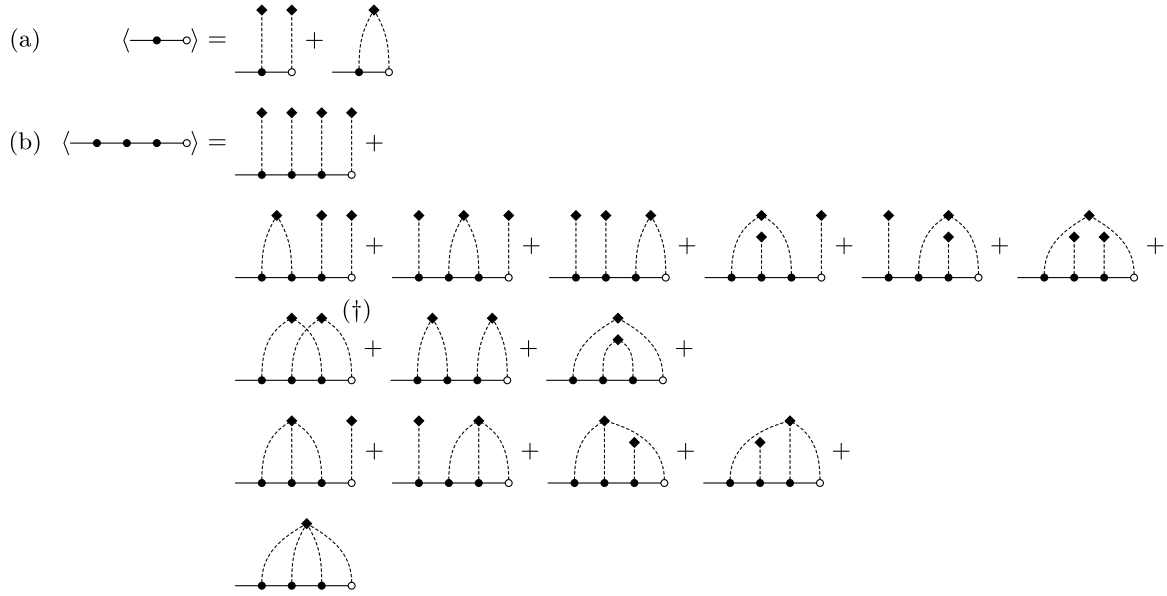


Figure 11. The second (a) and fourth (b) order term averages expanded using the diagrams. The bundles of dashed lines evaluate to cumulants \mathcal{C}^n . Crossed-cumulant terms (denoted with \dagger), are omitted in the coherent potential approximation. Other symbols are identical to those used in figure 10.

[77], we take advantage of the so-called cumulant expansion. For illustration, we consider again the second order term given by (24)

$$\begin{aligned} \langle \chi_{ij}^{\alpha\beta}(z, \mathbf{q}, \mathbf{q}') \rangle &= z^{-2} \tau_{(i)(m)}^{(l_1)}(\mathbf{q}, \mathbf{q}_1) \sigma_{(m)(j)}^{(l_2)} \\ &\times \langle \rho^{(l_1)}(\mathbf{q} - \mathbf{q}_1) \rho^{(l_2)}(\mathbf{q}_1 - \mathbf{q}') \rangle. \end{aligned} \quad (26)$$

Only the ρ functions contain random variables p , which must be averaged. The cumulant expansion of their product reads

$$\begin{aligned} \langle \rho^{(l_1)}(\mathbf{k}_1) \rho^{(l_2)}(\mathbf{k}_2) \rangle &= \mathcal{C}_{(l_1)(l_2)}^2(\mathbf{k}_1, \mathbf{k}_2) \\ &+ \mathcal{C}_{(l_1)}^1(\mathbf{k}_1) \mathcal{C}_{(l_2)}^1(\mathbf{k}_2), \end{aligned} \quad (27)$$

where \mathcal{C}^n denotes the multivariate cumulant of order n . For the case of uncorrelated disorder, we obtain

$$\begin{aligned} \mathcal{C}_{(l_1)(l_2)\dots(l_n)}^n(\mathbf{k}_1, \mathbf{k}_2, \dots, \mathbf{k}_n) &= \mathcal{P}_{(l_1)(l_2)\dots(l_n)}^n(\mathbf{c}) \\ &\times \Omega_{\text{BZ}} \delta(\mathbf{k}_1 + \mathbf{k}_2 + \dots + \mathbf{k}_n), \end{aligned} \quad (28)$$

where \mathbf{c} stands for the concentration matrix $c_{i\alpha}$ and \mathcal{P} are weight functions, which vanish only, if not all indices correspond to the same basis site. The latter does not seem to have any straightforward analytic representation but the first two read

$$\mathcal{P}_{i\alpha}^1(\mathbf{c}) = c_{i\alpha}, \quad (29)$$

$$\mathcal{P}_{i\alpha j\beta}^2(\mathbf{c}) = \delta_{ij} (\delta_{\alpha\beta} c_{i\alpha} - c_{i\alpha} c_{j\beta}). \quad (30)$$

From the momentum dependence of the cumulants follows, as implied by (25), that the averaged susceptibility is diagonal in the momentum variables and, as such, proportional to $\Omega_{\text{BZ}} \delta(\mathbf{q} - \mathbf{q}')$.

Two examples of the cumulant expansion are presented in figure 11. The coherent potential approximation omits terms involving ‘crossed’ cumulants. Terms of this type appear

starting from the fourth order average and are marked with \dagger in figure 11.

The final CPA expression for the averaged diagonal part $\langle \chi_{ij}^{\alpha\beta}(z, \mathbf{q}) \rangle$ of the susceptibility, see (25), involves the summation of the terms in all orders by means of a Dyson-like self-consistent equation. Because our diagrams feature two different types of vertices (\mathcal{T} and \mathcal{S}), two quantities appear, namely the CPA *effective medium propagator* $\mathcal{G}(z, \mathbf{q})$ and the *magnetic weight correction* $\mathcal{W}(z, \mathbf{q})$.

The propagator

$$\mathcal{G}(z, \mathbf{q}) = \Gamma(z) + \Gamma(z) \mathcal{E}(z, \mathbf{q}) \mathcal{G}(z, \mathbf{q}), \quad (31)$$

can be expressed in terms of the *self-energy* \mathcal{E}

$$\begin{aligned} \mathcal{E}(z, \mathbf{q}) &= \sum_{s \in S_1} \mathcal{P}_s^1 \tau^{(l_1)}(\mathbf{q}, \mathbf{q}) + \sum_{n=2}^{\infty} \sum_{s \in S_n} \mathcal{P}_s^n \\ &\times \int_{\mathbf{q}_1} \int_{\mathbf{q}_2} \dots \int_{\mathbf{q}_{n-1}} [\tau^{(l_1)}(\mathbf{q}, \mathbf{q}_1) \mathcal{G}(z, \mathbf{q}_1) \tau^{(l_2)}(\mathbf{q}_1, \mathbf{q}_2) \mathcal{G}(z, \mathbf{q}_2) \dots \\ &\dots \tau^{(l_{n-1})}(\mathbf{q}_{n-2}, \mathbf{q}_{n-1}) \mathcal{G}(z, \mathbf{q}_{n-1}) \tau^{(l_n)}(\mathbf{q}_{n-1}, \mathbf{q})], \end{aligned} \quad (32)$$

where $S_n \ni s = \{(l_1), (l_2), \dots, (l_n)\}$ is a particular sequence of composite indices of length n . Similarly, the weight correction \mathcal{W} can be calculated as

$$\begin{aligned} \mathcal{W}(z, \mathbf{q}) &= \sum_{s \in S_1} \mathcal{P}_s^1 \sigma^{(l_1)} + \sum_{n=2}^{\infty} \sum_{s \in S_n} \mathcal{P}_s^n \\ &\times \int_{\mathbf{q}_1} \int_{\mathbf{q}_2} \dots \int_{\mathbf{q}_{n-1}} [\tau^{(l_1)}(\mathbf{q}, \mathbf{q}_1) \mathcal{G}(z, \mathbf{q}_1) \tau^{(l_2)}(\mathbf{q}_1, \mathbf{q}_2) \mathcal{G}(z, \mathbf{q}_2) \dots \\ &\dots \mathcal{G}(z, \mathbf{q}_{n-1}) \sigma^{(l_n)}]. \end{aligned} \quad (33)$$

The final expression for the averaged susceptibility is the matrix product of the effective propagator and the weight correction

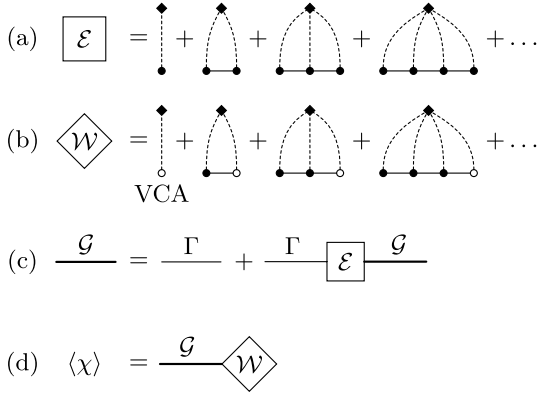


Figure 12. The Dyson equation for the CPA susceptibility in the diagrammatic representation. (a) CPA self-energy (32), (b) magnetic weight (33), (c) the Dyson equation (31), and (d) the final expression for the CPA susceptibility (34). The virtual crystal approximation is obtained by retaining the first terms in the series (a) and (b).

$$\langle \chi(z, \mathbf{q}) \rangle = \mathcal{G}(z, \mathbf{q}) \mathcal{W}(z, \mathbf{q}). \quad (34)$$

The expansion presented above is developed in terms of diagrams in figure 12. The calculations are necessarily self-consistent, as the effective medium propagator \mathcal{G} is obtained from the self-energy \mathcal{E} which in turn involves the propagator.

The series given by (32) and (33) do not converge when computed term-by-term. Furthermore, it is unfavourable from the computational point of view to work directly in the reciprocal space.

Below, we transform the necessary equations to the real space where the series can be summed over. For simplicity, we suppress the frequency arguments

$$\mathcal{E}(\mathbf{q}) = \mathcal{E}(\mathbf{q}, \mathbf{q}) \equiv \sum_{\mathbf{R}\mathbf{R}'} e^{-\mathbf{q} \cdot (\mathbf{R} - \mathbf{R}')} \mathcal{E}(\mathbf{R}, \mathbf{R}'), \quad (35)$$

$$\mathcal{W}(\mathbf{q}) \equiv \sum_{\mathbf{R}} e^{-\mathbf{q} \cdot \mathbf{R}} \mathcal{W}(\mathbf{R}), \quad (36)$$

$$\mathcal{E}(\mathbf{R}, \mathbf{R}') = \sum_{i\alpha} c_{i\alpha} \sum_{\mathbf{R}_1} \hat{\mathcal{E}}^{i\alpha}(\mathbf{R}, \mathbf{R}_1) \tau^{i\alpha}(\mathbf{R}_1, \mathbf{R}'), \quad (37)$$

$$\mathcal{W}(\mathbf{R}) = \sum_{i\alpha} c_{i\alpha} \hat{\mathcal{E}}^{i\alpha}(\mathbf{R}, \mathbf{0}) \sigma^{i\alpha}. \quad (38)$$

The *partial self-energies* $\hat{\mathcal{E}}$ are calculated as follows

$$\hat{\mathcal{E}}^i(\mathbf{R}, \mathbf{R}') = \sum_{\alpha \in I_i} \sum_{\mathbf{R}_1} c_{i\alpha} \hat{\mathcal{E}}^{i\alpha}(\mathbf{R}, \mathbf{R}_1) \mathcal{M}^{i\alpha}(\mathbf{R}_1, \mathbf{R}'), \quad (39)$$

where I_i is the set of impurity types present on site i . The terms off-diagonal in the sites' space vanish in the case of uncorrelated disorder. From now on, we will take advantage of matrices in a space of extended composite indices including both the composite index (i) as well as the lattice vector \mathbf{R} , i.e. $(\alpha i \mathbf{R})$. Only finite clusters of lattice vectors corresponding to the range of the exchange parameters $J(\mathbf{R})$ must be considered. Using the concept of the effective interaction

of Yonezawa, the summation of the cumulant series can be performed

$$c_{i\alpha} \hat{\mathcal{E}}^{i\alpha} = \mathcal{P}_{i\alpha}^1 \mathbb{1} + \mathcal{P}_{i\beta, i\alpha}^2 \mathcal{M}^{i\beta} + \mathcal{P}_{i\gamma, i\beta, i\alpha}^3 \mathcal{M}^{i\gamma} \mathcal{M}^{i\beta} + \dots \quad (40)$$

$$\hat{\mathcal{E}}^{i\alpha} = \left[\mathbb{1} - (\mathcal{M}^{i\alpha} - \hat{\mathcal{E}}^i) \right]^{-1}, \quad (41)$$

where the \mathcal{M} matrices are defined in the reciprocal space and read

$$\mathcal{M}_{(i)(j)}^{(l)}(\mathbf{q}, \mathbf{q}') = \tau_{(i)(m)}^{(l)}(\mathbf{q}, \mathbf{q}') \mathcal{G}_{(m)(j)}(\mathbf{q}'). \quad (42)$$

In the real space, they consist of two parts

$$\mathcal{M}_{(i)(j)}^{(l)}(\mathbf{R}, \mathbf{R}') = g S_{\alpha}^{-1} J_{ii}^{\alpha\gamma}(\mathbf{R}) \mathcal{G}_{(i)(j)}(\mathbf{R} - \mathbf{R}') - \sum_{\mathbf{R}_1} \left[g S_{\mu}^{-1} J_{lm}^{\gamma\mu}(\mathbf{R}_1) \mathcal{G}_{(m)(j)}(\mathbf{R}_1 - \mathbf{R}') \delta_{(i)(l)} \delta_{\mathbf{R}\mathbf{0}} \right]. \quad (43)$$

The equations above can be directly implemented in computer software to calculate $\langle \chi \rangle$. Several remarks concerning our numerical scheme are now in order. The convergence of the CPA self-consistency loop requires a careful mixing of quantities from previous iterations and we found that the Broyden method is suitable for that. Furthermore, the self-consistent loop does not converge when complex frequencies are located too close to the real axis. The latter difficulty can be circumvented using the nearly real axis method [58]. The self-consistent quantities are calculated in a suitable distance away from the real axis and subsequently the self-energy $\hat{\mathcal{E}}(z)$ is analytically continued towards the real energies in order to determine the quantities just above the real frequency axis.

5. Evaluation of exchange parameters in disordered systems

The exchange parameters entering the Heisenberg model (1) can be estimated from first-principles using the magnetic force theorem as it is implemented within the multiple-scattering theory. For an ordered system the exchange constants J_{ij} can be determined as shown in [40]

$$J_{ij} = \frac{1}{4\pi} \int_{\varepsilon_F}^{\varepsilon_F} d\varepsilon \text{Im Tr}_L \left[\Delta_i(\varepsilon) G_{\downarrow}^{ij}(\varepsilon) \Delta_j(\varepsilon) G_{\uparrow}^{ji}(\varepsilon) \right], \quad (44)$$

where Tr_L denotes the trace over the angular momentum, and it is integrated up to the Fermi energy ε_F . $G_{\sigma}^{ij}(\varepsilon)$ is the back scattering operator of a spin σ between the sites i and j , and $\Delta_i(\varepsilon) = t_{\uparrow}^i(\varepsilon) - t_{\downarrow}^i(\varepsilon)$ is defined via the single scattering t matrices $t_{\sigma}^i(\varepsilon)$ and closely related to the exchange splitting corresponding to the magnetic atom i . The Green function entering (44) can be calculated self-consistently using any implementation of the multiple scattering Green function method within the density functional theory [79–82].

The magnetic force theorem (44) can be generalized for disordered systems using the CPA [83, 84]

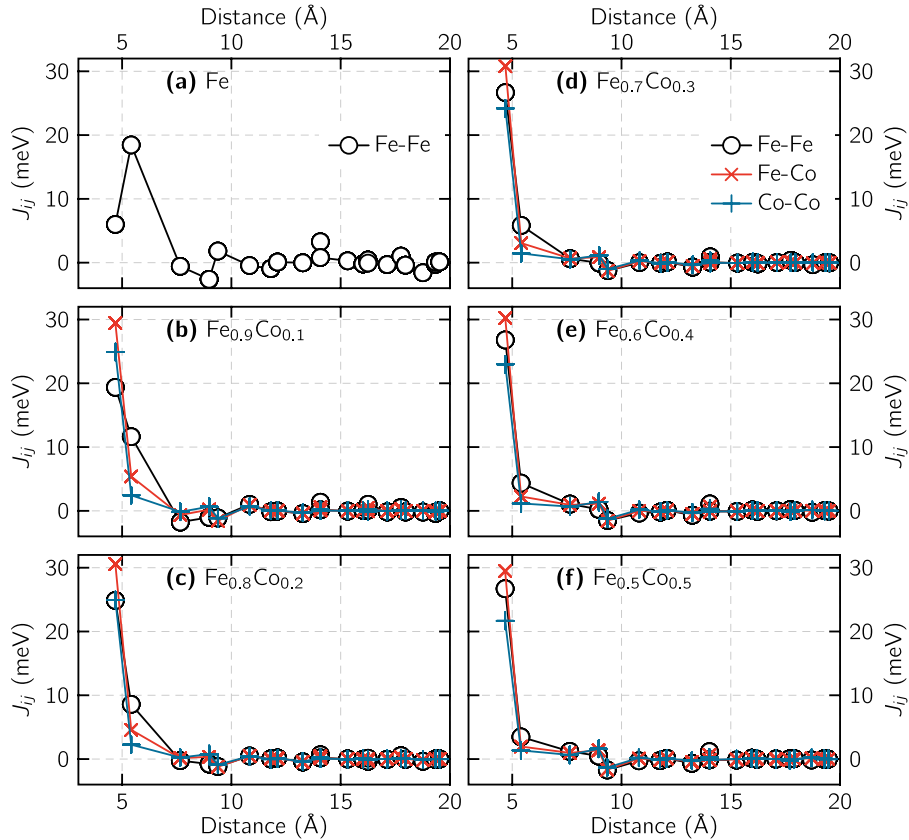


Figure 13. Distance dependent magnetic exchange parameters J_{ij} for Fe doped with Co calculated within the CPA as described in section 5: (a) pure Fe system, (b)–(f) Co concentration is raised by 10% up to 50%. The exchange parameters for Fe–Co and Co–Fe are the same.

$$J_{ij}^{\alpha\beta} = \frac{1}{4\pi} \int^{\varepsilon_F} d\varepsilon \text{Im Tr}_L \left[\Delta_i^\alpha(\varepsilon) (D_i^\alpha(\varepsilon))^\dagger G_\downarrow^{ij}(\varepsilon) D_j^\beta(\varepsilon) \times \Delta_j^\beta(\varepsilon) (D_j^\beta(\varepsilon))^\dagger G_\uparrow^{ji}(\varepsilon) D_i^\alpha(\varepsilon) \right], \quad (45)$$

where Greek letters denote again atomic types and $D_i^\alpha(\varepsilon)$ is the so-called impurity matrix corresponding to an impurity atom α on the site j [81]. The Green function in (45) is calculated self-consistently in a coherent medium $t_c(\varepsilon)$ and Fourier transformed into the real space.

6. Comparison of both schemes

It is reasonable to inquire how an essentially mean-field-like CPA (section 4) performs compared to the supercell simulations (section 3), i.e. a numerically exact scheme. The question has been already answered for dilute magnets, i.e. uncorrelated mixtures of magnetic and non-magnetic atoms [68]. In short, the CPA provides an excellent account of the spin wave spectra in the high-dimensional structures above the percolation threshold.

Here, we ask the same question for mixtures of only magnetic atoms and answer it based on the example of Co doped bulk Fe ($\text{Fe}_x\text{Co}_{1-x}$ alloys). We assume the uncorrelated disorder, i.e. an Fe atom is directly replaced with a probability $1 - x$ on a parent bcc lattice by a Co atom, irrespective of the occupation of other sites around or local lattice relaxations. The latter restriction follows from the usage of the CPA but is

well justified because we are substituting only atoms of comparable atomic radii on the bcc lattice. For the sake of simplicity, we do not consider other potential phases like an ordered B2 phase or short-ranged phases as discussed in [85]. The experimental lattice parameters given in Landolt–Börnstein [86] were interpolated in order to use them in our calculations at the desired Co concentrations—ranging from 0% to 50% in steps of 10%.

The electronic ground state of the system calculated with the CPA method, including the magnetic moments and the exchange constants J_{ij} , are determined from the density functional theory. The details concerning the calculations of the exchange constants are given in section 5. For the supercell scheme, we extended the primitive unit cell $16 \times 16 \times 16$ times and applied the Voronoi tessellation described in section 3.1.2.

The spin-wave spectrum of pure bcc-Fe has been thoroughly studied, see [58] and references therein. The dispersing spin waves form a single band. The energy of the least energetic magnon is zero—it is a Goldstone mode.

An introduction of Co to the parent lattice of Fe changes the magnetic system profoundly. The nearest neighbor Fe–Fe exchange interaction generally increase, while long ranged Fe–Fe J_{ij} values decrease. Hence, the systems become more short-ranged, and loose their tendency to anti-ferromagnetic coupling between further shells (figure 13). For larger Co concentrations ($\geq 40\%$), the Fe–Fe J_{ij} remain almost similar. The other magnetic coupling constants—Fe–Co and Co–Co—vary only slightly for different Co doping levels. These

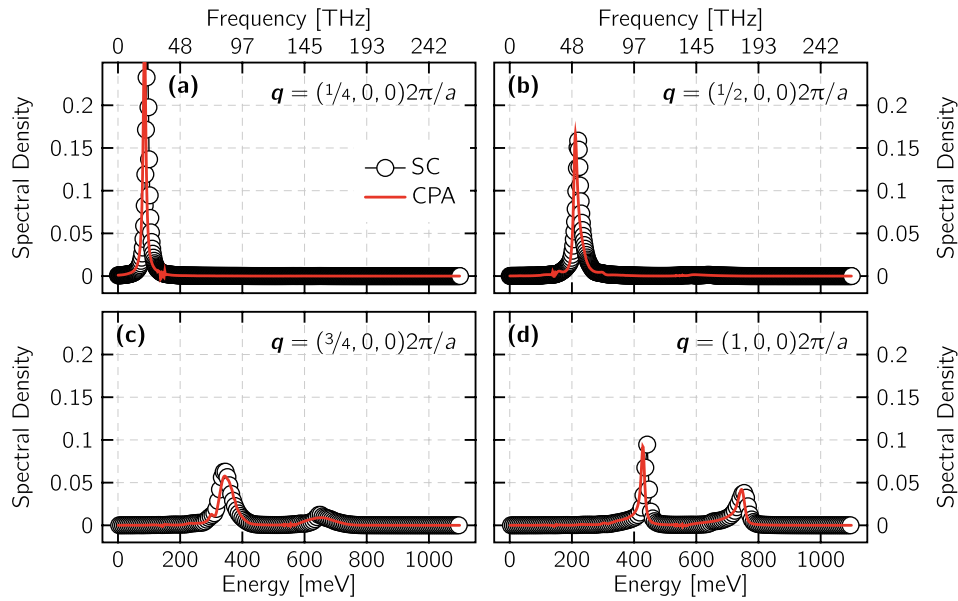


Figure 14. Magnonic spectrum of the $\text{Fe}_{0.9}\text{Co}_{0.1}$ alloy for different wave vectors along (100) direction. The spectra obtained with both methods—the CPA (red lines) or supercell (SC) scheme (black spheres)—are presented. Frequency range is estimated by $E = hf$ with Planck’s constant h .

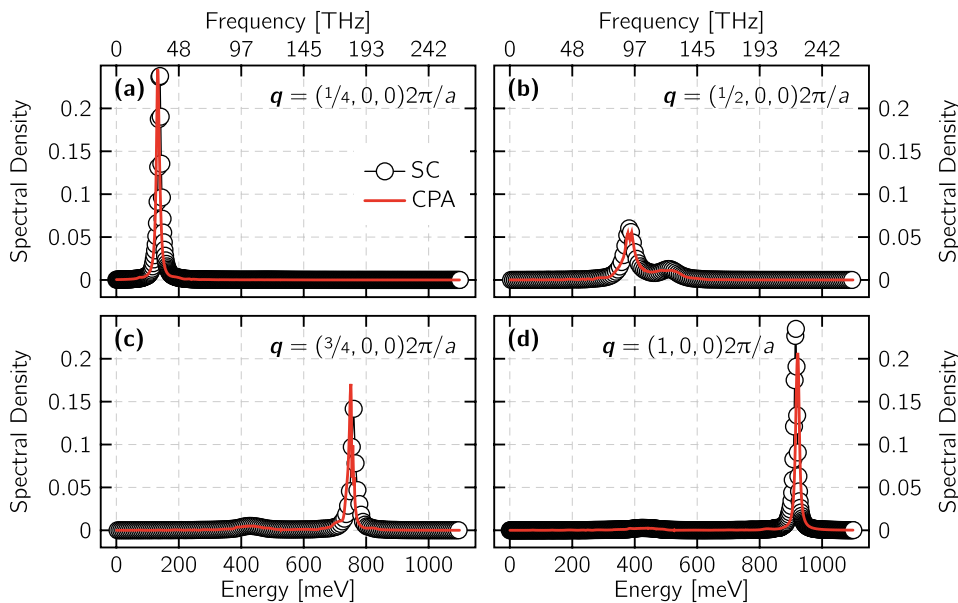


Figure 15. Magnonic spectrum of the $\text{Fe}_{0.5}\text{Co}_{0.5}$ alloy for different wave vectors along (100) direction. The spectra obtained with both methods—the CPA (red lines) or supercell (SC) scheme (black spheres)—are presented. Frequency range is estimated by $E = hf$ with Planck’s constant h .

variations result in general in a broader magnonic bandwidth and less non-monotonic dispersion relation compared to the pure bcc-Fe as shown for weakly Co-doped alloys ($x = 0.9$) and $\text{Fe}_{0.5}\text{Co}_{0.5}$ (figures 14 and 15, respectively). In addition, we observe a perfect match between the CPA and the supercell scheme.

Another important feature is the appearance of a new class of weakly dispersive magnonic states. These states appear for $x = 0.9$ above the continuum of acoustic magnons at around 700 meV (figure 14). They are clearly discernible for large wave vectors and the analysis of the corresponding magnonic modes (magnonic eigenvectors) in the real space clearly shows

that these new states are strongly localized on the Co impurities, while the modes in the acoustic continuum are generally delocalized and supported on the host Fe atoms (figure 16). The low energy mode considered in figure 16(a) belongs to the continuum of acoustic magnons, while the high energy mode in figure 16(b) is a member of the disorder induced weakly dispersive band forming above the acoustic continuum. In the high energy mode the amplitudes vary much more strongly between sites than in the low energy mode. As a consequence, the high energy mode is much more strongly localized—primarily on the Co impurities. On the other hand, the low energy mode is delocalized and supported primarily on the host Fe

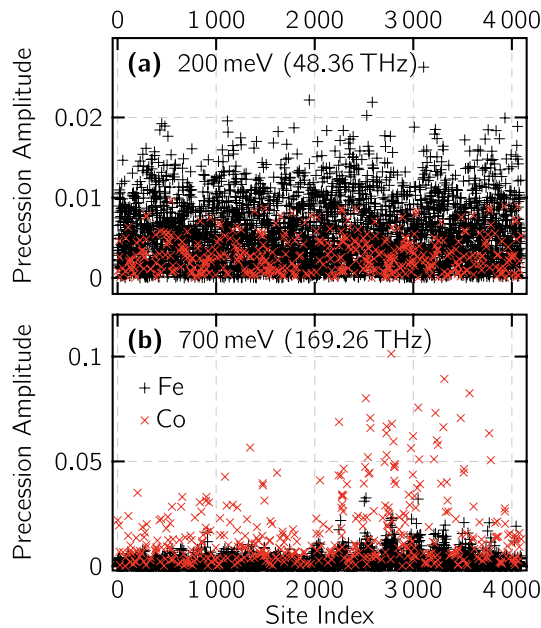


Figure 16. The precession amplitude of magnon states at (a) 200 meV and (b) 700 meV in the $\text{Fe}_{0.9}\text{Co}_{0.1}$ alloy. The analysis is performed in real space and the amplitude is shown as the function of the atom's position index in the cluster. One particular random realization of the supercell is considered, which allows to distinguish between the sites occupied by the Fe (black +) and Co (red \times) atoms. Frequency range is estimated by $E = hf$ with Planck's constant h .

atoms. It should be remarked that such analysis is straightforward in the case of supercell calculations.

The energy of these weakly dispersive magnon states gradually decreases with the increasing Co concentration. Around $x = 0.8$ the states appear within the dispersing acoustic band, close to its top (not shown). Around $x = 0.5$ they are located in the middle of the band at around 450 meV (figure 15). We can clearly observe how for $\mathbf{q} = (\frac{1}{2}, 0, 0)2\pi/a$ the more intense dispersing magnon state hybridizes with the weakly dispersing mode (figure 15(b)). Because of this hybridization the magnonic state associated with the weakly dispersing mode is far less localized for large Co concentrations than its counterpart above the acoustic band for small Co concentrations.

Another interesting observation is the non-monotonous dependence of the acoustic spin wave peak's width on the state's energy. Low energy magnons with small momenta and the states close to the top of the dispersing band are associated with relatively narrow spectral peaks, i.e. they are long living. On the contrary, the magnons with the intermediate momenta, appearing in the middle of the band, correspond to wider peaks signifying stronger damping.

It is gratifying to observe that the CPA performs surprisingly well despite its mean field character. It is able to capture not only the emergence of the dispersing acoustic spin wave modes but also the weakly dispersive magnonic features both above (for low impurity concentration) and within (for high impurity concentration) the acoustic band. Furthermore, the CPA predicts correctly the energies and widths of all these

magnon modes across the whole concentration range of Co impurities.

7. Summary

In this work, we presented our approach to determine the magnon properties in complex disordered magnetic systems. It is based on the adiabatic mapping of a spin system on the Heisenberg Hamiltonian, whereas the exchange integrals are computed from the *ab initio* density functional ground state. The disorder is treated with two complementary strategies. In the case of *uncorrelated* disorder one can resort to the CPA, which we systematically derived here for the Heisenberg model. It is shown that the approximation performs surprisingly well despite its mean field character. The other strategy is the direct numerical simulation of large supercells using configurational average over possible samples. This approach is computationally much more demanding (contrary to the semi-analytic CPA calculations) but allows to study systems featuring *correlated* disorder effects, including clustering and formation of islands in two-dimensional systems—two very common effects in real systems. It is shown that the inclusion of these effects is indispensable to the reliable theoretical interpretation of experimental results.

Acknowledgments

This publication was funded by the German Research Foundation (DFG) within the Collaborative Research Centre 762 (projects A4 and B1) and the priority program SPP 1538. KhZ acknowledges the support by the DFG through the Heisenberg Program ZA 902/3-1 and the DFG Grant No. ZA 902/4-1. We are grateful to L M Sandratskii and H Ibach for fruitful discussions.

ORCID iDs

Martin Hoffmann  <https://orcid.org/0000-0002-8426-725X>
 Timofey Balashov  <https://orcid.org/0000-0003-0966-7920>
 Khalil Zakeri  <https://orcid.org/0000-0002-4674-3446>

References

- [1] Bloch F 1930 *Z. Phys.* **61** 206
- [2] Holstein T and Primakoff H 1940 *Phys. Rev.* **58** 1098
- [3] Majlis N 2000 *The Quantum Theory of Magnetism* (Singapore: World Scientific)
- [4] Zakeri K 2014 *Phys. Rep.* **545** 47
- [5] Tyablikov S V 1967 *Methods in the Quantum Theory of Magnetism* (New York: Springer)
- [6] Kirilyuk A, Kimel A V and Rasing T 2010 *Rev. Mod. Phys.* **82** 2731
- [7] Cole H S D and Turner R E 1967 *Phys. Rev. Lett.* **19** 501
- [8] Costache M V, Bridoux G, Neumann I and Valenzuela S O 2012 *Nat. Mater.* **11** 199
- [9] Liu J P, Fullerton E, Gutfleisch O and Sellmyer D J (ed) 2009 *Nanoscale Magnetic Materials and Applications* (New York: Springer)

- [10] Onose Y, Ideue T, Katsura H, Shiomi Y, Nagaosa N and Tokura Y 2010 *Science* **329** 297
- [11] Woolsey R B and White R M 1970 *Phys. Rev. B* **1** 4474
- [12] Lévy L P 2000 *Magnetism and Superconductivity* (Heidelberg: Springer)
- [13] Essenberger F, Buczek P, Ernst A, Sandratskii L and Gross E K U 2012 *Phys. Rev. B* **86** 060412
- [14] Essenberger F, Sanna A, Buczek P, Ernst A, Sandratskii L and Gross E K U 2016 *Phys. Rev. B* **94** 014503
- [15] Shirane G, Shapiro S M and Tranquada J M 2002 *Neutron Scattering with a Triple-Axis Spectrometer: Basic Techniques* (Cambridge: Cambridge University Press)
- [16] Chatterji T 2005 *Neutron Scattering from Magnetic Materials* (Amsterdam: Elsevier)
- [17] Grünberg P 1985 *Prog. Surf. Sci.* **18** 1
- [18] Hillebrands B, Baumgart P and Güntherodt G 1989 *Appl. Phys. A* **49** 589
- [19] Balashov T, Takács A F, Wulfhekel W and Kirschner J 2006 *Phys. Rev. Lett.* **97** 187201
- [20] Balashov T, Takács A F, Däne M, Ernst A, Bruno P and Wulfhekel W 2008 *Phys. Rev. B* **78** 174404
- [21] Gao C L, Ernst A, Fischer G, Hergert W, Bruno P, Wulfhekel W and Kirschner J 2008 *Phys. Rev. Lett.* **101** 167201
- [22] Balashov T, Buczek P, Sandratskii L, Ernst A and Wulfhekel W 2014 *J. Phys.: Condens. Matter* **26** 394007
- [23] Rado G T and Weertman J R 1959 *J. Phys. Chem. Solids* **11** 315
- [24] Plihal M, Mills D L and Kirschner J 1999 *Phys. Rev. Lett.* **82** 2579
- [25] Vollmer R, Etzkorn M, Kumar P S A, Ibach H and Kirschner J 2003 *Phys. Rev. Lett.* **91** 147201
- [26] Etzkorn M, Anil Kumar P, Vollmer R, Ibach H and Kirschner J 2004 *Surf. Sci.* **566** 241
- [27] Prokop J, Tang W X, Zhang Y, Tudosa I, Peixoto T R F, Zakeri K and Kirschner J 2009 *Phys. Rev. Lett.* **102** 177206
- [28] Zakeri K, Zhang Y, Prokop J, Chuang T H, Sakr N, Tang W X and Kirschner J 2010 *Phys. Rev. Lett.* **104** 137203
- [29] Zakeri K, Zhang Y, Chuang T H and Kirschner J 2012 *Phys. Rev. Lett.* **108** 197205
- [30] Qin H J, Zakeri K, Ernst A, Chuang T H, Chen Y J, Meng Y and Kirschner J 2013 *Phys. Rev. B* **88** 020404
- [31] Meng Y, Zakeri K, Ernst A, Chuang T H, Qin H J, Chen Y J and Kirschner J 2014 *Phys. Rev. B* **90** 174437
- [32] Qin H J, Zakeri K, Ernst A, Sandratskii L M, Buczek P, Marmodoro A, Chuang T H, Zhang Y and Kirschner J 2015 *Nat. Commun.* **6** 6126
- [33] Zakeri K 2017 *J. Phys.: Condens. Matter* **29** 13001
- [34] Ibach H, Rajeswari J and Schneider C M 2011 *Rev. Sci. Instrum.* **82** 123904
- [35] Ibach H and Rajeswari J 2012 *J. Electron. Spectrosc. Relat. Phenom.* **185** 61
- [36] Rajeswari J, Ibach H and Schneider C M 2013 *Europhys. Lett.* **101** 17003
- [37] Michel E, Ibach H, Schneider C M, Santos D L R and Costa A T 2016 *Phys. Rev. B* **94** 014420
- [38] Michel E, Ibach H and Schneider C M 2016 *Surf. Interface Anal.* **48** 11047
- [39] Rajeswari J, Ibach H and Schneider C M 2014 *Phys. Rev. Lett.* **112** 127202
- [40] Liechtenstein A I, Katsnelson M I, Antropov V P, Gubanov V A, Gubanov V A and Gubanov V A 1987 *J. Magn. Magn. Mater.* **67** 65
- [41] Gyorffy B L, Pindor A J, Staunton J, Stocks G M and Winter H 1985 *J. Phys. F: Met. Phys.* **15** 1337
- [42] Staunton J B, Gyorffy B L, Pindor A J, Stocks G M and Winter H 1985 *J. Phys. F: Met. Phys.* **15** 1387
- [43] Sandratskii L M 1998 *Adv. Phys.* **47** 91
- [44] Bergman A, Taroni A, Bergqvist L, Hellsvik J, Hjörvarsson B and Eriksson O 2010 *Phys. Rev. B* **81** 144416
- [45] Taroni A, Bergman A, Bergqvist L, Hellsvik J and Eriksson O 2011 *Phys. Rev. Lett.* **107** 037202
- [46] Bergqvist L, Taroni A, Bergman A, Etz C and Eriksson O 2013 *Phys. Rev. B* **87** 144401
- [47] Eriksson O, Bergman A, Bergqvist L and Hellsvik J 2016 *Atomistic Spin Dynamics: Foundations and Applications* (Oxford: Oxford University Press)
- [48] Etz C, Bergqvist L, Bergman A, Taroni A and Eriksson O 2015 *J. Phys.: Condens. Matter* **27** 243202
- [49] Runge E and Gross E K U 1984 *Phys. Rev. Lett.* **52** 997
- [50] Gross E K U and Kohn W 1985 *Phys. Rev. Lett.* **55** 2850
- [51] Stenzel E and Winter H 1985 *J. Phys. F: Met. Phys.* **15** 1571
- [52] Savrasov S Y 1990 *Solid State Commun.* **74** 69
- [53] Savrasov S Y 1998 *Phys. Rev. Lett.* **81** 2570
- [54] Staunton J B, Poulter J, Ginatempo B, Bruno E and Johnson D D 2000 *Phys. Rev. B* **62** 1075
- [55] Grotheer O, Ederer C and Fähnle M 2001 *Phys. Rev. B* **63** 100401
- [56] Buczek P, Ernst A, Bruno P and Sandratskii L M 2009 *Phys. Rev. Lett.* **102** 247206
- [57] Buczek P A 2009 Spin dynamics of complex itinerant magnets *PhD Thesis* Martin Luther Universität Halle-Wittenberg
- [58] Buczek P, Ernst A and Sandratskii L M 2011 *Phys. Rev. B* **84** 174418
- [59] Lounis S, Costa A T, Muniz R B and Mills D L 2011 *Phys. Rev. B* **83** 035109
- [60] Soven P 1967 *Phys. Rev.* **156** 809
- [61] Gyorffy B L 1972 *Phys. Rev. B* **5** 2382
- [62] Matsubara T 1973 *Progr. Theor. Phys. Suppl.* **53** 202
- [63] Theumann A 1974 *J. Phys. C: Solid State Phys.* **7** 2328
- [64] Bouzerar G and Bruno P 2002 *Phys. Rev. B* **66** 014410
- [65] Bouzerar G, Kudrnovský J, Bergqvist L and Bruno P 2003 *Phys. Rev. B* **68** 081203
- [66] Bouzerar G, Ziman T and Kudrnovský J 2005 *Phys. Rev. B* **72** 125207
- [67] Tang G X and Nolting W 2006 *Phys. Rev. B* **73** 024415
- [68] Buczek P, Sandratskii L M, Buczek N, Thomas S, Vignale G and Ernst A 2016 *Phys. Rev. B* **94** 054407
- [69] Thomas S 2017 Multiple scattering approach for excitations in complex systems *PhD Thesis* Martin-Luther-Universität Halle-Wittenberg
- [70] Balashov T 2009 Inelastic scanning tunneling spectroscopy: magnetic excitations on the nanoscale *PhD Thesis* Universität Karlsruhe (TH)
- [71] Durstenfeld R 1964 *Commun. ACM* **7** 420
- [72] Perlin K 1985 *ACM SIGGRAPH Comput. Graph.* **19** 287
- [73] Perlin K 2002 *ACM Trans. Graph.* **21** 681
- [74] Perlin K 2005 Standard for perlin noise *US Patent* no. US6867776B2 www.google.com/patents/US6867776
- [75] Meyerheim H L, Popescu R and Kirschner J 2006 *Phys. Rev. B* **73** 245432
- [76] Zakeri K, Chuang T H, Ernst A, Sandratskii L M, Buczek P, Qin H J, Zhang Y and Kirschner J 2013 *Nat. Nanotechnol.* **8** 853
- [77] Yonezawa F and Morigaki K 1973 *Progr. Theor. Phys. Suppl.* **53** 1
- [78] Blackman J A, Esterling D M and Berk N F 1971 *Phys. Rev. B* **4** 2412
- [79] Gyorffy B L and Stott M J 1973 *Theory of Soft X-Ray Emission from Alloys* (London: Academic) p 385
- [80] Lüders M, Ernst A, Temmerman W M, Szotek Z, Durham P J, Lüders M, Ernst A, Temmerman W M, Szotek Z and Durham P J 2001 *J. Phys.: Condens. Matter* **13** 8587
- [81] Ebert H, Ködderitzsch D and Minár J 2011 *Rep. Prog. Phys.* **74** 096501

- [82] Geilhufe M, Achilles S, Köbis M A, Arnold M, Mertig I, Hergert W and Ernst A 2015 *J. Phys.: Condens. Matter* **27** 435202
- [83] Turek I, Kudrnovský J, Drchal V, Bruno P and Blügel S 2003 *Phys. Status Solidi* **236** 318
- [84] Turek I, Kudrnovský J, Drchal V and Bruno P 2006 *Phil. Mag.* **86** 1713
- [85] Abrikosov I A, James P, Eriksson O, Söderlind P, Ruban A V, Skriver H L and Johansson B 1996 *Phys. Rev. B* **54** 3380
- [86] Hellwege K H and Hellwege A M (ed) 1971 *Structure Data of Elements and Intermetallic Phases (Landolt-Börnstein—Group III Condensed Matter vol 6)* (Berlin: Springer)
- [87] Chen *et al* 2017 *Phys. Rev. Lett.* **119** 267201